SPE-193818-MS

A Compositional Model for Gas Injection IOR/EOR in Tight Oil Reservoirs Under Coupled Nanopore Confinement and Geomechanics Effects

Ye Tian, Yi Xiong, and Lei Wang, Colorado School of Mines; Zhengdong Lei and Yuan Zhang, Research Institute of Petroleum Exploration and Development, PetroChina; Xiaolong Yin and Yu-Shu Wu, Colorado School of Mines

This paper was prepared for presentation at the SPE Reservoir Simulation Conference held in Galveston, Texas, USA, 10–11 April 2019.

Abstract

Gas injection has become the top choice for IOR/EOR pilots in tight oil reservoirs because of its high injectivity. The effects of nanoconfinement and geomechanics are generally considered as non-negligible, but its coupled effects and resulting flow and displacement are still not well understood for gas injection. We hence present a general compositional model and simulator to investigate the complicated multiphase and multicomponent behaviors during gas injection in tight oil reservoirs.

This compositional model is able to account for vital physics in unconventional reservoirs, including nanopore confinement, molecular diffusion, rock-compaction, and non-Darcy flow. The MINC method is implemented to handle fractured media. The nanopore confinement effect is modeled by including capillarity in VLE calculations. The rock compaction effect is represented by solving the mean stress from a governing geomechanical equation which is fully coupled with the mass balance equations to ensure the numerical stability as well as a physically correct solution. The equations are discretized with integral finite difference method and then solved numerically by Newton's method.

The simulator is validated against a commercial compositional software (CMG-GEM) before it is applied to simulate gas injection. Huff-n-puff with dry gas in Eagle Ford is investigated. The simulation result shows that if the reservoir pressure is much higher than the bubble point pressure, the nanopore confinement effect will have a minimal impact on the recovery factor (RF) for both the depletion and the first few cycles of gas huff-n-puff. Geomechanics is found to be an influencing factor on RF but not always in a detrimental way, as enhanced rock compaction drive could offset the reduction of permeability in certain scenarios. Gas huff-n-puff would improve the RF of each component compared with the depletion. The heavy component would first have a higher recovery than the light component at the first few cycles of huff-n-puff, but its RF will be outpaced by the light component when the gas saturation in the matrix surpasses the critical gas saturation. Lastly, considering the nanopore confinement effects would slightly reduce the RF of the light component but increase the RF of the heavy component after huff-n-puff when combined with the critical gas saturation effect in the matrix.

This study presents a 3D multiphase, multicomponent simulator which is a practical tool for accurately modeling of primary depletion as well as gas injection IOR/EOR processes in unconventional oil reservoirs.

This simulator is not only of great importance for assisting researchers to understand complex multiphase and multicomponent behaviors in tight oil production but also of great use for engineers to optimize gas injection parameters in field applications.

Introduction

As of 2017, about 54% of the total oil produced in the United States were contributed by tight reservoirs, and this number is predicted to be around 70% in the 2040s (EIA, 2018). Unconventional oil producing basins such as Bakken, Eagle Ford, Permian, and Niobrara have drawn significant attention within the global oil industry over the last decade. Currently, the best practice to produce tight oil is through primary depletion using multistage hydraulically fractured horizontal wells, but the recovery factors are deficient, typically less than 10% (Hoffman and Evans, 2016) due to the nature of unconventional reservoirs. For example, in Bakken despite the application of horizontal drilling and multistage hydraulic fracturing, the oil recovery factor is still about 4 to 6%. (Hawthorne et al. 2013). Also, unconventional oil wells are characterized by a fast decline rate between 50% and 70% during the first year of production (Wang et al., 2017). With the large volume of oil in place in unconventional reservoirs such as Bakken (7.4 billion recoverable reserves), the success of IOR practice with even a minor improvement of 1 % would lead to an enormous increase in oil production.

Over the past few years, many methods have been proposed for IOR/EOR in tight oil reservoirs based on theoretical research and laboratory studies (Kurtoglu et al. 2013; Gamadi et al. 2014), some of which have been applied in pilot tests (Sheng, 2015). So far, the most promising IOR/EOR technologies for tight oil reservoirs seems to favor gas injection (hydrocarbon gas, CO_2, N_2, etc.), because gas often has a higher compressibility and a lower viscosity than liquid, leading to higher injectivity and energy supplement potentials for tight formations. The immiscible gas injection can supply reservoir with additional energy meanwhile the dissolution of gas would make oil phase lighter and less viscous (Peng et al., 2017). For a miscible process, besides the above mechanisms, IFT between injected gas and oil could be dramatically reduced even eliminated which would significantly increase microscopic displacement efficiency. Lastly, for tight reservoirs, gas causes less formation damage than liquid injection. Therefore, gas injection including hydrocarbon and non-hydrocarbon gas has become the first choice for research and pilot tests for enhancing oil recovery from unconventional reservoirs. Gas huff-n-puff is often favored compared with flooding because of the easiness of single-well operation and shorter response time (Wang et al., 2017).

Though a black oil model could be implemented for modeling IOR/EOR in tight oil reservoirs such as water flood or immiscible gas injection, compositional modeling based on an equation of state is becoming a favored approach in most recent published studies. This is mainly because black oil models could not accurately handle the transport process (Qiao, 2015) if it is highly compositional dependent especially when transport is dominated by diffusion in the tight matrix or when capillary confinement might shift the Vapor-Liquid Equilibrium (VLE), let alone when these effects are coupled with geomechanics. Several compositional models for tight oil reservoirs considering complex physics have been established, but they mainly focused on primary depletion (Xiong, 2015; Uzun et al., 2018). Many simulation studies for gas EOR in tight oil reservoirs have been done, but most of them are either based on conventional compositional models (Chen et al., 2014; Wan et al., 2016) or commercial software (Hoffman et al., 2014; Sheng and Chen, 2014; Sanchez-Rivera et al., 2014; Yu et al., 2015; Phi and Schechter, 2017;) where the effects of complex physics are less studied, e.g., coupled stress and capillary confinement effects. This paper presents a fully-implicit compositional model which couples nanopore confinement and geomechanical effects during gas injection in tight oil reservoirs. Our simulation results using this model reveals some insightful multiphase and multicomponent behaviors, which could only be understood with a compositional simulator with coupled nanopore confinement effect and geomechanics.

Compositional Modelling

The compositional model in this paper is based on the framework initially developed by (Wu, 2015; Xiong, 2015). Nc+1 mass balance equations correspond with Nc+1 components. Among them, Nc equations are for the components existing in both oil and gas phase which can be pure hydrocarbon, non-hydrocarbon (e.g., CO_2 or N_2) or pseudo components as long as the thermodynamic properties required by EOS are specified.

$$-\nabla\cdot\left(\rho_o x_i \vec{v}_o + \rho_g y_i \vec{v}_g\right) + \nabla\cdot\left[D_{eff,i}\nabla\left(\rho_g y_i\right)\right] + q_i = \frac{\partial\left[\phi(\rho_o S_o x_i + \rho_g S_g y_i)\right]}{\partial t} \quad \text{Eq. 1}$$

The last mass balance equation is for the water component, which is assumed to be present only in the aqueous phase.

$$-\nabla\cdot\left(\rho_w \vec{v}_w\right) + q_w = \frac{\partial(\phi\rho_w S_w)}{\partial t} \quad \text{Eq. 2}$$

The partial differential equations are integrated within the arbitrary REV (representative elementary volume) by following the integral finite difference (IFD) method which is essentially equivalent to the finite-volume method (Pruess, 1991).

$$\int_{V_n} -\nabla\cdot\left(\rho_o x_i \vec{v}_o + \rho_g y_i \vec{v}_g\right)\mathrm{d}V + \int_{V_n}\nabla\cdot\left[D_{eff,i}\nabla\left(\rho_g y_i\right)\right]\mathrm{d}V + \int_{V_n} q_i \mathrm{d}V = \int_{V_n}\frac{\partial\left[\phi(\rho_o S_o x_i + \rho_g S_g y_i)\right]}{\partial t}\mathrm{d}V \quad \text{Eq. 3}$$

Where V_n represents the volume of a grid block. By applying the divergence theorem, volume integrals are converted to surface integrals.

$$\int_{S_n} -\left(\rho_o x_i \vec{v}_o + \rho_g y_i \vec{v}_g\right)\cdot\boldsymbol{n}\mathrm{d}S + \int_{S_n} D_{eff,i}\nabla\left(\rho_g y_i\right)\cdot\boldsymbol{n}\mathrm{d}S + \int_{V_n} q_i \mathrm{d}V = \int_{V_n}\frac{\partial\left[\phi(\rho_o S_o x_i + \rho_g S_g y_i)\right]}{\partial t}\mathrm{d}V \quad \text{Eq. 4}$$

Where S_n denotes the surface area of a grid block, and $\boldsymbol{n}$ is the outward normal unit vector that describes the spatial orientation of dS. Thermodynamic properties of fluids and rock are represented by averages over explicitly defined grid blocks, while mass fluxes across surface segments between connected grid blocks are evaluated by finite difference approximations. The time discretization is implemented using a backward, first-order finite difference method. Finally, the discretized equations are written in the residual form and ready to be solved by Newton iterations.

$$\begin{aligned} R_{i,n}^{t+1} = {} & \frac{\left[V\phi(\rho_o S_o x_i + \rho_g S_g y_i)\right]_n^{t+1} - \left[V\phi(\rho_o S_o x_i + \rho_g S_g y_i)\right]_n^{t}}{\Delta t} \\ & - \sum_{m\in\eta_n}\left[\left(\rho_o x_i \lambda_o\right)_{nm+1/2}^{t+1}\gamma_{nm}^{t+1}\left(\Phi_{om}^{t+1} - \Phi_{on}^{t+1}\right) + \left(\rho_g y_i \lambda_g\right)_{nm+1/2}^{t+1}\gamma_{nm}^{t+1}\left(\Phi_{gm}^{t+1} - \Phi_{gn}^{t+1}\right)\right] \\ & - \sum_{m\in\eta_n}\left[D_{eff,i}A_{nm}^{t+1}\frac{\left(\rho_g y_i\right)_m^{t+1} - \left(\rho_g y_i\right)_n^{t+1}}{d_n^{t+1} + d_m^{t+1}}\right] - \left(Vq_i\right)_n^{t+1} \end{aligned} \quad \text{Eq. 5}$$

Similarly, the residual form of mass balance equation for aqueous phase can be written as,

$$R_{w,n}^{t+1} = \frac{\left[V\phi\rho_w S_w\right]_n^{t+1} - \left[V\phi\rho_w S_w\right]_n^{t}}{\Delta t} - \sum_{m\in\eta_n}\left[\left(\rho_w\lambda_w\right)_{nm+1/2}^{t+1}\gamma_{nm}^{t+1}\left(\Phi_{wm}^{t+1} - \Phi_{wn}^{t+1}\right)\right] - \left(Vq_w\right)_n^{t+1} \quad \text{Eq. 6}$$

Where Φ_{nm} is the flow potential of a phase; λ_{nm} is the mobility with upstream weighting; γ_{nm} is the transmissibility between two connected grids and defined as,

$$\gamma_{nm}^{t+1} = \left(\frac{A_{nm} k_{nm+1/2}}{d_n + d_m} \right)^{t+1} \quad \text{Eq. 7}$$

Where A_{nm} is the common interface area between connected grid n and m; d_n is the distance from the center of grid n to the interface between grid n and m; $k_{nm+1/2}$ is the harmonic averaged absolute permeability along the connection between grid n and m as shown in Figure 1.

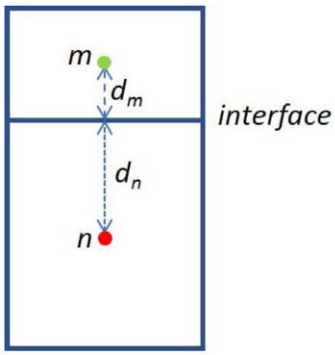

Figure 1—Connection between two neighboring grids

Geomechanics

The geomechanical formulation in this model is based on the previous work by Winterfeld and Wu (2016). From the classical poro-thermal-elastic theory,

$$\boldsymbol{\sigma} - \alpha p\mathbf{I} - 3\beta K\Delta T = 2G\boldsymbol{\varepsilon} + \lambda(tr\boldsymbol{\varepsilon})\mathbf{I} \quad \text{Eq. 8}$$

Where $\boldsymbol{\sigma}$ is the stress tensor; $\mathbf{I}$ is the identity matrix; α is Biot's coefficient; β is the linear thermal expansion coefficient; K is the bulk modulus; G is shear modulus; λ is Lame's first parameter. Also, we have the relationship between the displacement vector $\boldsymbol{\varepsilon}$ and the strain tensor $\mathbf{u}$,

$$\boldsymbol{\varepsilon} = \frac{1}{2}\left(\nabla\mathbf{u} + \nabla\mathbf{u}^{\mathrm{T}}\right) \quad \text{Eq. 9}$$

Then the static mechanical equilibrium equation can be written as,

$$\nabla \cdot \boldsymbol{\sigma} + \mathbf{F}_b = 0 \quad \text{Eq. 10}$$

We then can combine Eq. 8, 9, and 10 and have the poro-thermal-elastic Navier Equation.

$$\nabla(\alpha P + 3\beta K\Delta T) + (\lambda + G)\nabla(\nabla \cdot \mathbf{u}) + G\nabla^2\mathbf{u} + \mathbf{F}_b = 0 \quad \text{Eq. 11}$$

Taking the divergence of Eq. 11 leads to

$$\nabla^2(\alpha P + 3\beta K\Delta T) + (\lambda + 2G)\nabla^2(\nabla \cdot \mathbf{u}) + \nabla \cdot \mathbf{F}_b = 0 \quad \text{Eq. 12}$$

The trace of the stress tensor is an invariant, and based on Eq. 8 it can be written as,

$$K\varepsilon_v = \sigma_{\mathrm{mean}} - (\alpha P + 3\beta K\Delta T) \quad \text{Eq. 13}$$

Where σ_{mean} is the average of normal stress tensor component, which corresponds to the uniform confining stress in laboratory experiments (Zoback, 2010); ε_v is the volumetric strain. Since the divergence of the displacement vector is the volumetric strain, we can combine Eq. 12 and Eq. 13,

$$\nabla \cdot \left[\nabla(\alpha P + 3\beta KT) + \frac{\lambda + 2G}{K}\nabla(\sigma_{mean} - \alpha P - 3\beta K\Delta T) + \mathbf{F}_b \right] = 0 \quad \text{Eq. 14}$$

In this paper, since the reservoir is assumed to be isothermal, we can simplify Eq. 14 as,

$$\nabla \cdot \left[\nabla(\alpha P) + \frac{\lambda + 2G}{K} \nabla(\sigma_{mean} - \alpha P) + \mathbf{F}_b \right] = 0 \quad \text{Eq. 15}$$

K, G, and λ can be expressed as the combination of Young's modulus E and Poisson's ratio v, and we finally have

$$\nabla \cdot \left[\frac{3(1-\nu)}{1+\nu} \nabla \sigma_{mean} - \frac{2(1-2\nu)}{1+\nu} \nabla(\alpha P) + \mathbf{F}_b \right] = 0 \quad \text{Eq. 16}$$

The above equation can be seen as conservation of momentum,

$$\nabla \cdot \psi = 0 \quad \text{Eq. 17}$$

Where ψ is the momentum flux. To handle different geomechanical properties in the neighboring grids n and m, the momentum flux between them can be evaluated with rock properties of two different girds respectively using the finite difference approximation, i.e., one calculated using properties and primary variables at the node m, and the other using properties and primary variables at the node n (Winterfeld and Wu, 2018).

$$\psi_{m,\text{int}} \cdot \boldsymbol{n} = \frac{3(1-\nu_m)}{1+\nu_m} \frac{\sigma_m - \sigma_{nm+1/2}}{d_m} + \mathbf{F}_{b,m} \cdot \boldsymbol{n} - \frac{2\alpha_m(1-2\nu_m)}{1+\nu_m} \frac{P_m - P_{nm+1/2}}{d_m} \quad \text{Eq. 18}$$

$$\psi_{\text{int},n} \cdot \boldsymbol{n} = \frac{3(1-\nu_n)}{1+\nu_n} \frac{\sigma_{nm+1/2} - \sigma_n}{d_n} + \mathbf{F}_{b,\text{n}} \cdot \boldsymbol{n} - \frac{2\alpha_n(1-2\nu_n)}{1+\nu_n} \frac{P_{nm+1/2} - P_n}{d_n} \quad \text{Eq. 19}$$

Where $\boldsymbol{n}$, the normal unit vector of the interface can either be towards node n or m, but must be consistent for the same interface). The above two fluxes are identical due to the continuity assumption,

$$\psi_{m,\text{int}} \cdot \boldsymbol{n} = \psi_{\text{int},n} \cdot \boldsymbol{n} = \psi_{mn} \cdot \boldsymbol{n}$$

We can then erase the mean stress at the interface $\sigma_{\text{nm+1/2}}$ by manipulating Eq. 18 and Eq. 19 and have,

$$\psi_{mn} = [\sigma_m - \sigma_n + \frac{(1+\nu_m)d_m}{3(1-\nu_m)} \mathbf{F}_{b,m} \cdot \boldsymbol{n} - \frac{(1+\nu_n)d_n}{3(1-\nu_n)} \mathbf{F}_{b,n} \cdot \boldsymbol{n} - \frac{2(1-2\nu_m)}{3(1-\nu_m)} \alpha_m (P_m - P_{nm+1/2}) - \frac{2(1-2\nu_n)}{3(1-\nu_n)} \alpha_n (P_n - P_{nm+1/2})] \Big/ \left(\frac{(1+\nu_m)d_m}{3(1-\nu_m)} + \frac{(1+\nu_n)d_n}{3(1-\nu_n)} \right) \quad \text{Eq. 20}$$

Like the mass balance equation, we could write the residual form of discretized mean stress equation as,

$$R_{\sigma,n}^{t+1} = \sum_{m \in \eta_n} \psi_{mn}^{t+1} A_{nm}^{t+1} \quad \text{Eq. 21}$$

The fluid flow is coupled with geomechanics by solving Eq. 21 simultaneously with mass balance equations. We can then calculate all the components in the stress tensor once the mean stress is solved by Eq. 21 (Winterfeld and Wu, 2016). As mentioned above, Nc+2 governing equations have been established to solve for Nc+2 primary variables, which are water saturation S_w, oil phase pressure P_o, overall mole fraction $Z_1, \ldots, Z_{Nc-1}$ for the components existing in both oil and gas phase and mean stress σ_{mean}.

VLE calculation with the nanopore confinement

Once the primary variables are solved by Newton's iteration, the VLE (Vapor-Liquid Equilibrium) calculation subroutine is called to calculate the saturation of gas and oil phase, as well as the mole fraction of both phases. In tight reservoirs, the sizes of pore and pore-throat in the matrix are in the scale of nanometers (Nelson, 2009), which might lead to a substantial capillary pressure between liquid and vapor phase at equilibrium and hence affect the VLE calculation. Firincioglu et al. (2012) studied the pore confinement effect on thermodynamic phase behaviors by including capillary pressure and van der Waals forces in the VLE calculation. It is found that the contribution of the surface forces is very small compared to the capillary force on the influence of phase behaviors. Similar studies also showed that nanopore confinement could further affect other thermodynamic properties such as viscosity, density, the minimum miscibility pressure, etc. (Teklu et al., 2014; Wang et al., 2016). Experimental studies based on nanofluidics also witnessed that the deviation of the saturation pressure of hydrocarbons in nanochannels (Wang et al. 2014; Parsa et al., 2015). The influence of nanopore confinement on primary depletion has been investigated by many researchers, and generally, it is recognized as favorable in a black oil system due to suppressed bubble point (Alharthy et al., 2016). In gas condensate system, the increased dew point pressure may lead to a negative impact, but it is less pronounced as the IFT is often small between a gas-like liquid and its corresponding vapor phase (Shapiro and Stenby, 2001). The main difference between the VLE calculation without confinement and the VLE calculation with confinement is the treatment of phase pressure. Instead of treating phase pressure the same, the VLE with confinement would consider their difference caused by the capillary pressure,

$$f_i^L = \phi_i^L x_i P_L = f_i^V = \phi_i^V y_i P_V \Rightarrow K_i = \frac{y_i}{x_i} = \frac{P_L \phi_i^L}{P_V \phi_i^V} = \frac{P_L \phi_i^L}{(P_L + P_c)\phi_i^V}$$

The VLE calculation algorithm used in this study is modified based previous work by Xiong (2015). Previous work focused on the depletion process, the bubble point pressure calculation subroutine is called only when the pressure of a grid is smaller than bubble point pressure P_b plus a tolerance value $\Delta P_{tor,}$ e.g. 145 psi or 1 MPa

$$P_o < P_b + \Delta P_{tor} \qquad \text{Eq. 22}$$

Then the code will proceed with a standard two-phase P-T flash. This method would work well for the primary depletion of a black-oil reservoir. However, for a gas injection case or depletion of a volatile oil or condensate gas reservoir, such criteria for phase stability would fail. In this study, instead of calculating saturation pressure which costs the same computationally as the VLE calculation, a negative flash algorithm (Whitson and Michelson, 1989; Wang et al., 2014) is used. Limiting the liquid mole faction L within the interval [0, 1] is relaxed to [1/(1-K_{max}), 1/(1-K_{min})] which would be more robust for a component e.g., condensate gas. Relaxing the solution interval of L could still guarantee a physical value during fugacity by Peng-Robinson EOS and interfacial tension σ_{og} calculated by Katz et al. (1943),

$$\sigma_{og}^{1/4} = \sum_{1}^{N_c} \chi_i (\rho_o x_i - \rho_g y_i) \qquad \text{Eq. 23}$$

Where the parachor of a component χ_i can be estimated by Weinaug and Katz (1943). Once the negative flash with nanopore confinement effects is converged, secondary variables such as L, molar composition of the liquid phase $x_1,\ldots,x_{Nc-1}$, molar composition of vapor phase $y_1,\ldots,y_{Nc-1}$ need to be ensured in the physical range for the next step of calculating the residual of governing equations. For example, if L is smaller than 0, then for a single-phase vapor, the molar fraction of a components in the liquid x_i, liquid phase density and saturation need to be reset as 0 and y_i needs to be set as z_i for the purpose of mass balance instead of using the results returned directly from the negative flash subroutine.

Coupling of nanopore confinement and geomechanics

The needs for coupling stress and nanopore confinements is because that capillary pressure between oil and gas is often determined by the Young-Laplace equation (Danesh, 1998),

$$P_c = \frac{2\sigma_{og}\cos\theta}{r(\sigma')} \quad \text{Eq. 24}$$

Where the pore radius r is often a function of effective stress $\sigma' = \sigma_{mean} - \alpha P$. The dominant pore radius can generally be expressed as a function of stress-dependent permeability and porosity.

$$r = C_1\left[\frac{k(\sigma')}{\phi(\sigma')}\right]^{C_2} \quad \text{Eq. 25}$$

Where C_1 is a factor based on the pore geometry. Because of the requirement of dimensional consistency (Tian et al., 2019), we often use C_2 as 0.5. For the stress-dependent porosity, a correlation developed by McKee et al. (1988) is used in this study,

$$\phi = \phi_0 \frac{e^{-c_p\Delta\sigma'}}{1-\phi_0(1-e^{-c_p\Delta\sigma'})} \quad \text{Eq. 26}$$

For the stress-dependent permeability, an exponential decay model is mostly applicable based on related experimental studies (Cho et al., 2013; Tian, 2014),

$$k = k_0 e^{-C_3\Delta\sigma'} \quad \text{Eq. 27}$$

If C_3 is not available from experiments, McKee et al. (1988) suggested using $C_3 = 3c_p$. The coupling process exists in two levels. Firstly, the geomechanics is coupled with the flow when solving for primary variables. Also, the VLE calculation with nanopore confinement is coupled with stress-dependent rock properties, whose algorithm is shown in Figure 2. The blue shaded area is where certain secondary variables mentioned above are not within the physical range, but such treatments could provide more robustness especially for considering nanopore confinement effect near the phase boundary. The unphysical value of secondary variables will be corrected accordingly once PT flash converges. Then the corrected secondary variables will be plugged into the governing equations for the next Newton's iteration, which is vital for the mass balance equations.

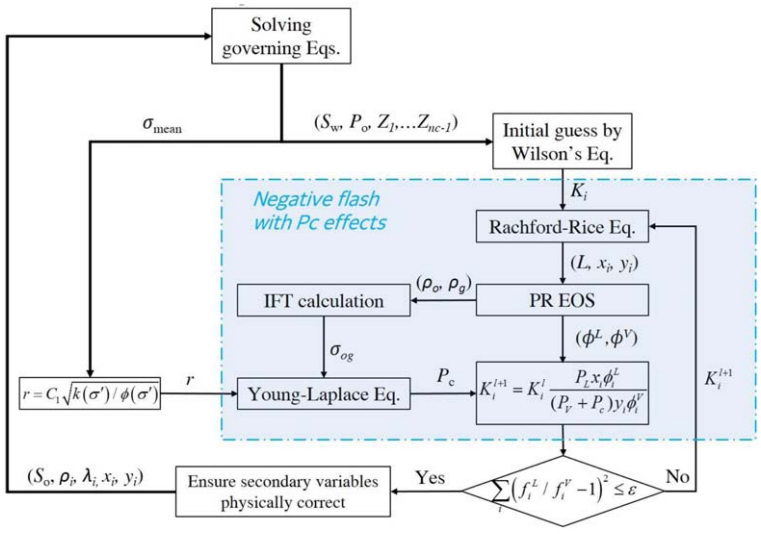

Figure 2—Coupling of nanopore confinement and geomechanics in VLE calculation

Simulation of Gas Huff-n-Puff

Description of the base case

The conceptual model for the base case is shown in Figure 3, which consists of the stimulated reservoir volume (SRV) and the unstimulated rock. Within the SRV, there is a hydraulic fracture stage with three perforation clusters. The planar hydraulic fracture is modeled explicitly by logarithmically refined local grids near the hydraulic fracture face. Within a hydraulic fracture, it is assumed that the fracture tip region is unpropped therefore has a smaller width and conductivity (Cheng, 2012), and is more sensitive to the effective stress change than the propped part of a hydraulic fracture. To model the activated natural fractures in the SRV, MINC (Multiple INteracting Continua) is used. It has been shown by previous studies (Wang and Narasimhan, 1985; Wu and Pruess, 1988) that both dual porosity and dual permeability model agree well with MINC and each of them can be treated as a special case of MINC with only two sub-grids. The unstimulated reservoir rock is also handled with MINC as a fractured medium, but with a lower permeability. Due to the symmetric nature of the conceptual model, only half of the model is needed for the simulation. Key dimensions of the model are based on data from published studies (Gong et al., 2013; Wan et al., 2016; Phi and Schechter, 2017). The geometry of the base case is summarized in Table 1.

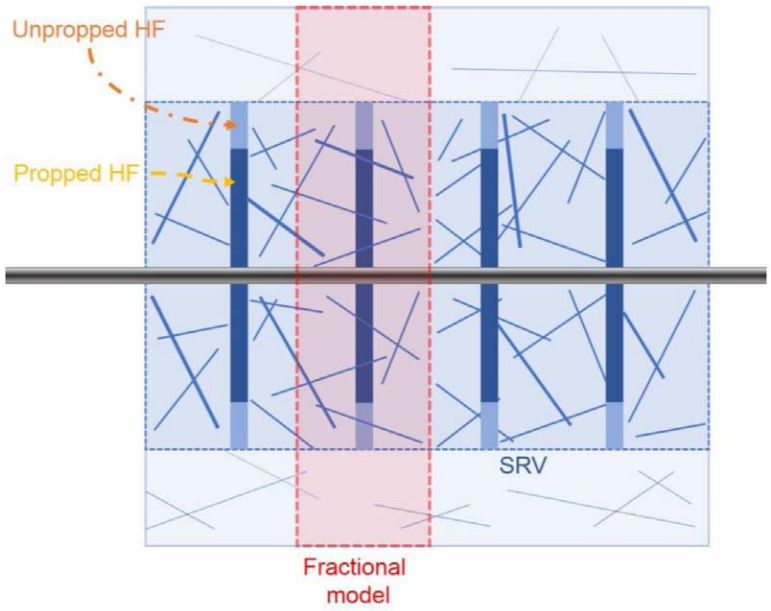

Figure 3—Schematic of the conceptual reservoir model

Table 1—Geometry of the base case for reservoir simulation

Well geometry		Fractional model	
Perforated lateral length, ft	6840	X, ft	90
Stage number	19	Y, ft	650
Clusters per stage	4	Z, ft	100
Cluster spacing, ft	90	Fracture half-length, ft	210
Formation thickness, ft	100	Fracture height, ft	36

The grid system of the fractional model is shown in Figure 4. Three layers are defined vertically with a total thickness as 100 ft, where the hydraulic fracture is assumed to be contained in the second layer and it has the same size in K direction as the propped fracture height of 36 ft. The width of the model is 90 ft in

I direction, which is the same as the cluster spacing. The length of the model is 650 ft, which is half of the horizontal well spacing. The shaded grids represent the hydraulic fracture which has a total half-length of 210 ft, of which 180 ft is assumed to be supported by proppants. The grids close to HF face in I direction and close to the fracture tip in J direction were both logarithmically refined. After the refinement, the model has 7, 12, 3 grids in I, J, K direction respectively. The active grid number for the base case is 504 because each primary grid has two sub-grids, i.e., natural fracture and matrix.

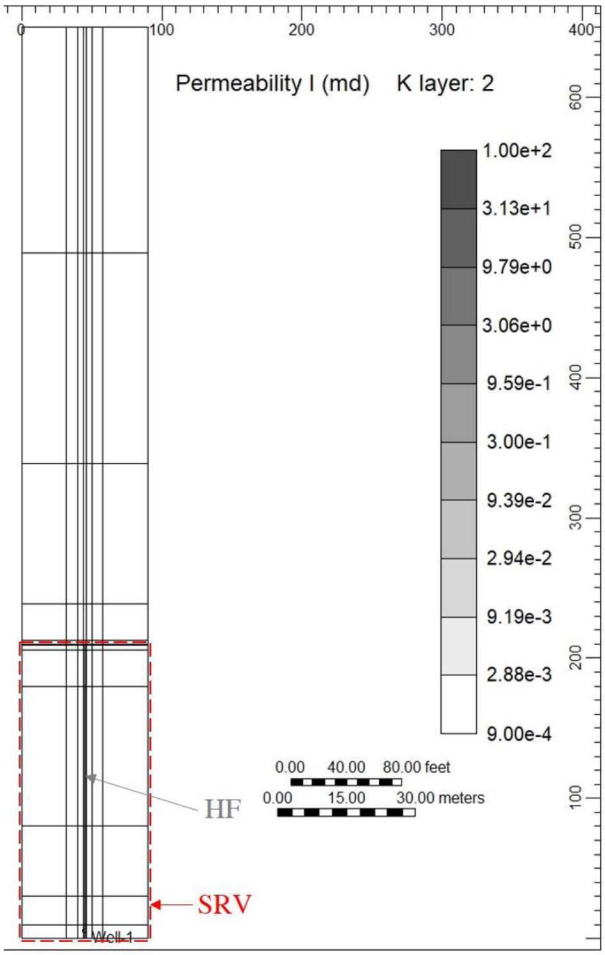

Figure 4—The grid system in the I-J plane for the base case

In the conceptual model, there are five different porous media including propped hydraulic fractures (HF), unpropped hydraulic fractures, natural fractures (NF) in SRV, NF outside SRV and the matrix. The area circled by the red dash line in Figure 4 is the SRV whose natural fracture media are assumed to be reactivated, and hence have a higher permeability than the natural fracture outside SRV. The hydraulic properties of different porous media are specified based on previous studies (Chaudhary et al., 2011; Phi and Schechter, 2017; Yu et al., 2018) and are summarized in Table 2. Since the hydraulic fracture is modeled explicitly by logarithmically refined local grids, and the grid width w_{grid} containing HF as 2 ft is much larger than the actual width of HF w_{HF} as 0.001 ft. The grid effective permeability k_{HFeff} is scaled accordingly to maintain the same fracture conductivity as specified (CMG, 2016).

$$k_{HFeff} = \frac{k_{HF} w_{HF}}{w_{grid}} \quad \text{Eq. 28}$$

Table 2—The hydraulic properties of different porous media

Rock types	Properties	Value
Propped HFs	Permeability, mD	2.0×10^{5}
	Width, ft	1.0×10^{-3}
	Porosity, %	50
Unpropped HFs	Permeability, mD	1.0×10^{5}
	Width, ft	3.0×10^{-4}
	Porosity, %	5
NFs in SRV	Permeability, mD	9.0×10^{-1}
	Porosity, %	0.12
	Spacing, ft	10×10×10
NFs outside SRV	Permeability, mD	4.5×10^{-2}
	Porosity, %	0.12
	Spacing, ft	10×10×10
Matrix	Permeability, mD	9.0×10^{-4}
	Porosity, %	12

For example, the grid effective permeability for the propped HF is 100 mD, which is obtained by dividing the propped HF's conductivity (200 mD-ft) with the grid width (2 ft). The reservoir is initially at 8125 psi and 240 °F. Initial water saturation is 17% in both the matrix and fracture network.

The geomechanical properties of different porous media are estimated based on Mokhtari et al. (2014) and are summarized in Table 1. It is noted that the fracture is set as less stiff than the matrix, with a smaller Young's modulus, but higher compressibility and Biot's coefficient assuming it is more stress-dependent than the matrix. The mean stress is assumed to be 9645 psi based on the data published by Guo et al. (2018) and the mean stress is assumed to be constant at the boundary.

The compositions of the reservoir oil are based on the published data (Yu et al., 2018), where six pseudo components are used to represent a typical light oil composition in the Eagle Ford shale as shown inTable 4. The bubble point p_b and GOR above p_b estimated by CMG-WinProp is 1585 psi and 943.6 scf/stb.

The relative permeability curves for matrix were based on the published data (Yu et al., 2018) and were smoothened by CMG before use as shown in Figure 5.

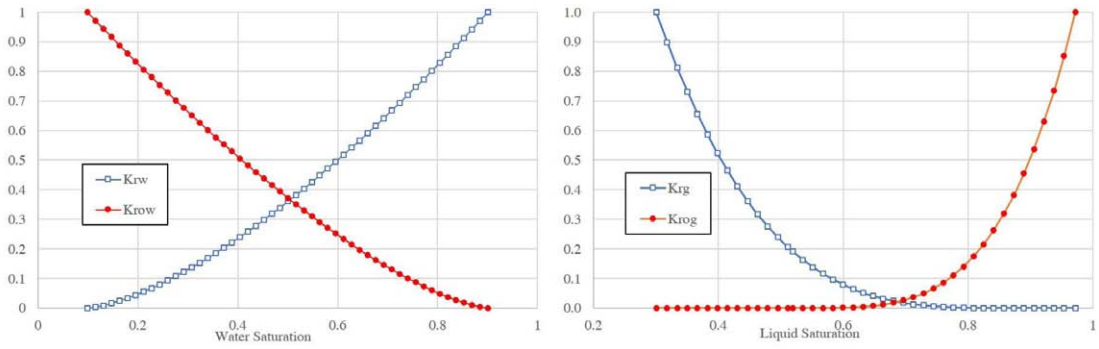

(a) Water-oil kr curve (b) Liquid-gas kr curve

Figure 5—The relative permeability curve for the matrix

The relative permeability curves within the fracture networks were generated and smoothened by assuming minimal residual saturation for all phases as shown in Figure 6. The same relative permeability

curves were used in all cases in this study. The critical gas saturation was set as 0.050 in the fracture network which was lower than that in the matrix as 0.127.

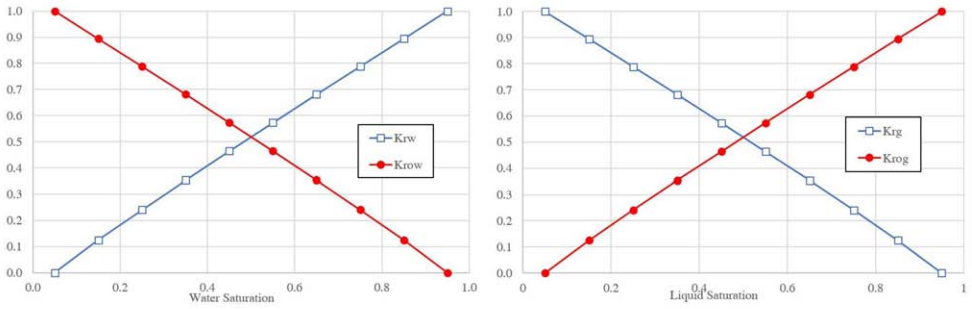

a) Water-oil kr curve (b) Liquid-gas kr curve

Figure 6—The relative permeability curve for the fracture network

Model validation

The base case was built and simulated with both CMG-GEM and our in-house compositional simulator MSFLOW-COM. Since CMG-GEM neither account for capillary condensation nor is fully coupled with geomechanics, the validation case built with MSFLOW-COM did not account for both effects either. The well was first depleted for 720 days and was then put on a gas huff-n-puff process. The molar composition of injected gas is 91% CH_4, and 9% CO_2, assuming all C2+ components are effectively recovered in the produced gas. The gas was being injected into the reservoir for 150 days with a constant rate of 1033.6 Mscf/day, which is almost equal to the total gas produced in the previous depletion. The well was shut-in for 30 days after injection. Finally, the well was put on constant BHP production for another 180 days.

The daily oil rate for 1081 days was multiplied by a factor of 152 because the fractional model only represented a 1/152 fraction of the entire well. The result was then compared with CMG-GEM as shown in Figure 7. Since the lowest BHP is 1824 psi which is above the bubble point, the GOR calculated from MSFLOW-COM is a constant as 947.5 scf/stb which is close to CMG-GEM's value as 943.6 scf/stb. For the pressure and oil saturation at the fracture grid containing the wellbore, there was no need to scale and the results were also compared with CMG-GEM and shown in Figure 8. MSFLOW-COM could obtain a very close result compared with CMG-GEM for both the depletion and gas huff-n-puff stage, which verified our compositional model as well as the correctness of the numerical approach to solve the model. Besides, MSFLOW-COM has been verified against experimental data, analytical solutions in the previous work by Xiong et al. (2015).

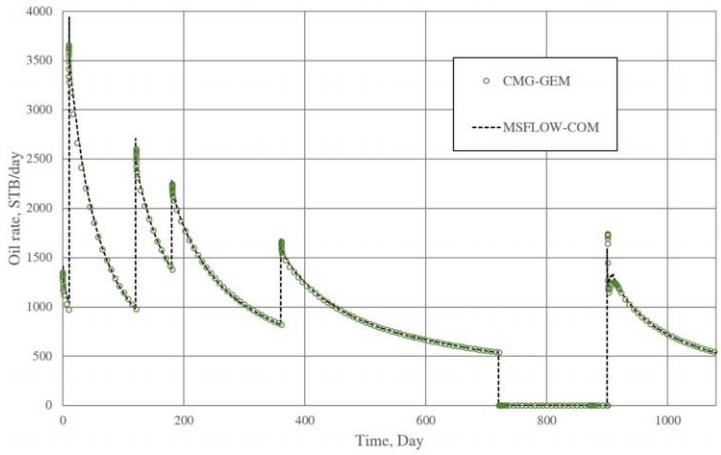

Figure 7—Comparison of the daily oil rate between CMG-GEM and MSFLOW-COM

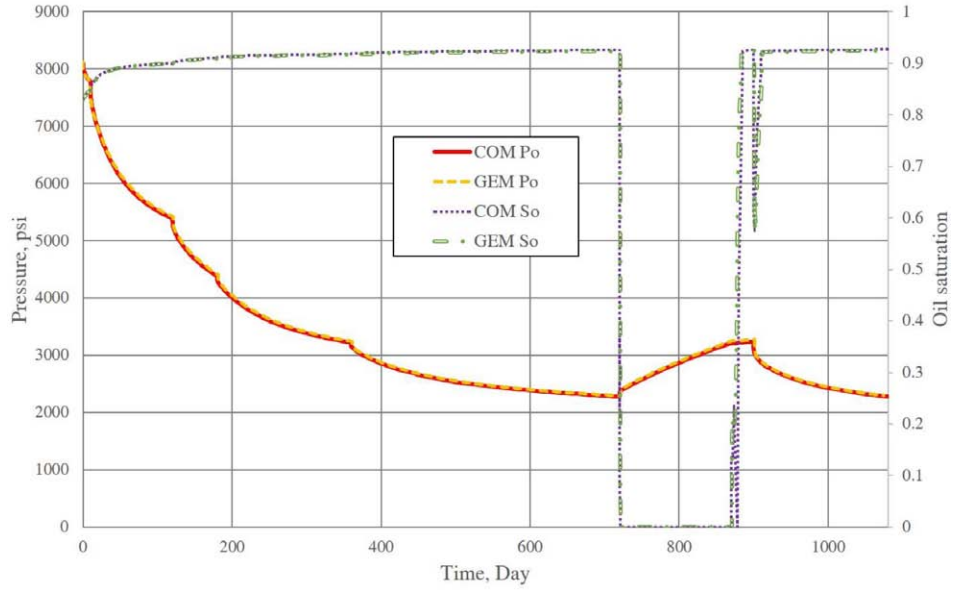

Figure 8—Comparison of the oil saturation and pressure at the grid containing the perforation

Results and Discussions

Besides the base case (Case #1, Base), several other cases were built and run with MSFLOW-COM. Case #2 (Geo) included the geomechanical effects i.e. simultaneously solving the stress equation and considering stress-dependent porosity, permeability, and rock volume. Case #3 (Pc) accounted for the nanopore confinement effect in the VLE module but not geomechanical effects. Case #4 (Geo+Pc) coupled the nanopore confinement and geomechanics effects. All cases in this study did not account for the molecular diffusion effect although it is available as an option in MSFLOW-COM. The recovery factors for CH_4 and C2-5 component were plotted in Figure 9 and Figure 10. Because CH_4 was the major component of the injected gas, its RF would decline during the huff-n-puff. For this specific reservoir, it seems nanopore confinement effect has a very limited impact on the RF during both depletion and the first cycle of gas huff-n-puff. However, coupling the geomechanics with flow would apparently affect the RF for both CH_4 and C2-5.

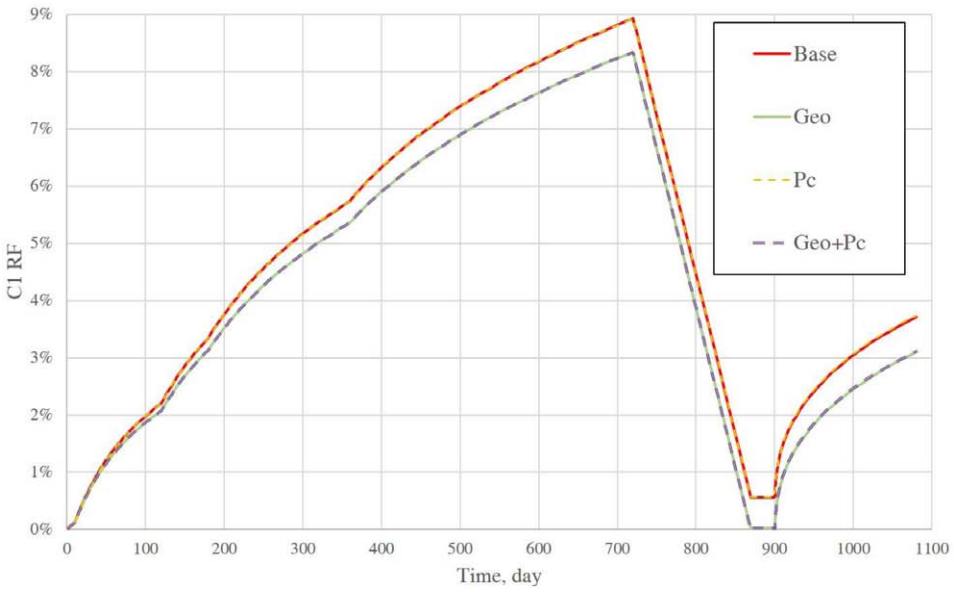

Figure 9—Comparison of the RF of CH_4 component among Case #1-4

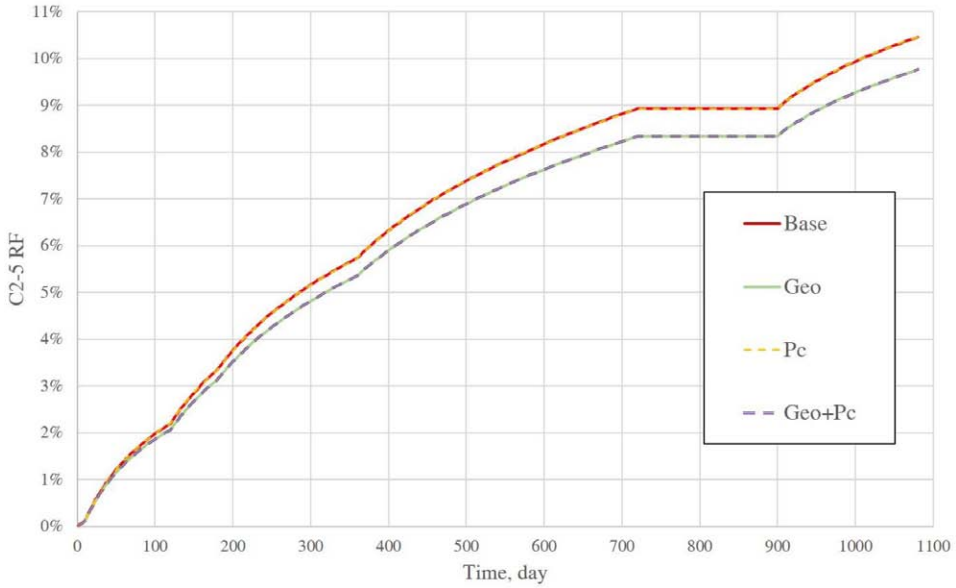

Figure 10—Comparison of the RF of C2-5 component among Case #1-4

In Case# 5, 6, different values of C_1 in Eq. 21 were specified (C_1=2, 5), which essentially represents different dominant pore sizes and its capillary effect on VLE calculation. C_1 was used as 10 in the base case which will lead to an effective matrix pore radius as 27 nm. By comparison among Case #2 (without capillary effect, C_1=∞, r=∞), Case #3 (C_1=10, r=27 nm), Case #5 (C_1=2, r=5.4 nm) and Case #6 (C_1=5, r=13.5 nm), we could see that the nanopore confinement effect has very limited influence on a component's recovery factor as shown in Figure 11 and Figure 12. The main reason is that during the depletion, the reservoir pressure was maintained above the bubble point and there was no free gas in the matrix. For the first cycle of gas huff-n-puff, the injected gas would only be mobile in the fracture networks which have a very large dominant pore size (>100nm), where the nanopore confinement effect is negligible.

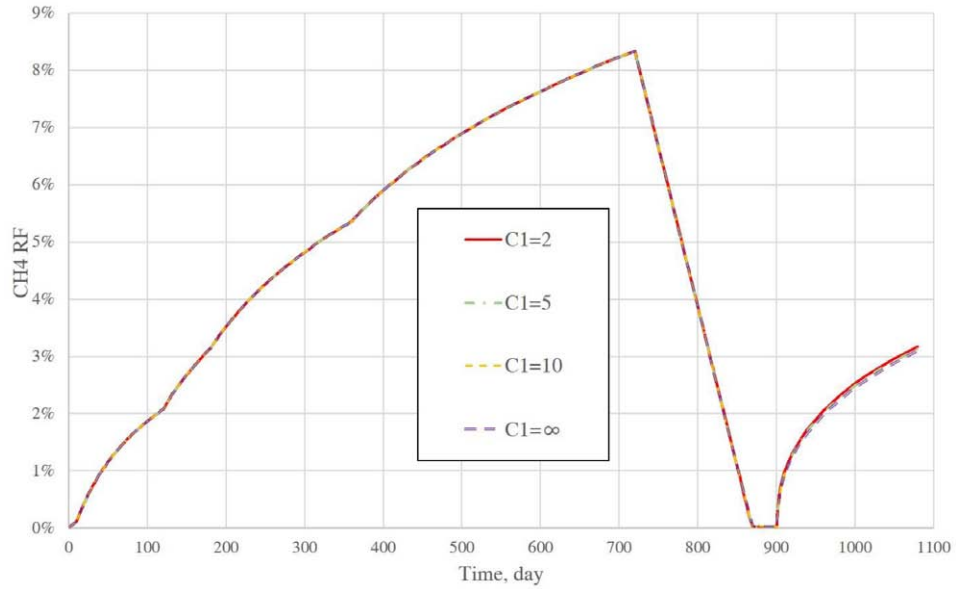

Figure 11—Comparison of the RF of CH_4 component with different pore sizes

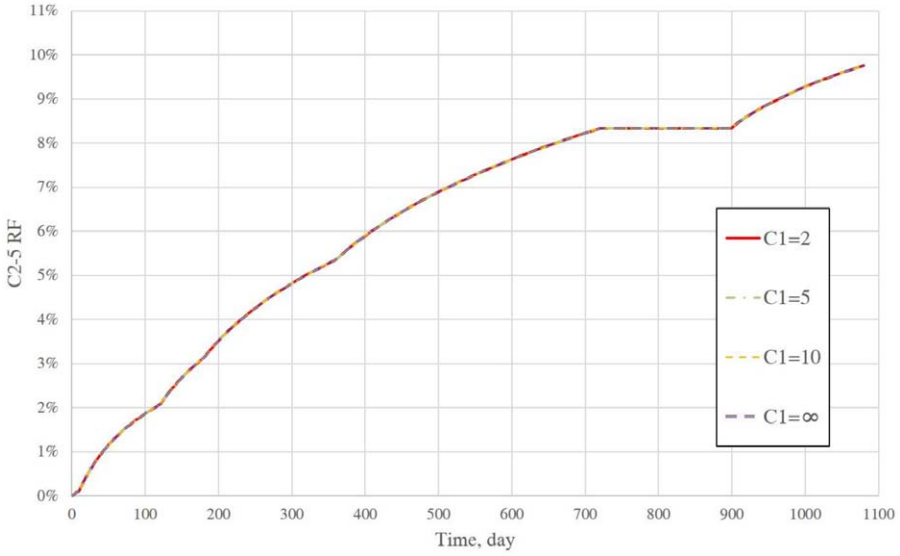

Figure 12—Comparison of the RF of C2-5 component with different pore sizes

On the basis of Case #4, Case #7 and #8 investigated the effect of Biot's coefficient of fracture media. Case #7 assumed that all fracture media had the same Biot's coefficient as 0.5 and Case #8 assumed that all fracture media had the same Biot's coefficient as 1. Case #4 specified different Biot's coefficient for different media as shown in Table 3 which could be treated as an intermedia scenario between Case #7 and #8. With a larger Biot's coefficient, the change of pore pressure should have a larger impact on the effective stress. With increasing Biot's coefficient, the RF for both CH_4 and C2-5 would be reduced, possibly due to decreased permeability in the fracture network.

Table 3—The geomechanical properties of different porous media

Rock types	Properties	Value
Propped HFs	Compressibility, psi^{-1}	7.5×10^{-6}
	Young's Modulus, psi	1.0×10^{6}
	Poisson's ratio	0.26
	Biot's coefficient	0.9
Unpropped HFs	Compressibility, psi^{-1}	7.5×10^{-6}
	Young's Modulus, psi	1.0×10^{6}
	Poisson's ratio	0.26
	Biot's coefficient	0.8
NFs in SRV	Compressibility, psi^{-1}	7.5×10^{-6}
	Young's Modulus, psi	1.5×10^{6}
	Poisson's ratio	0.26
	Biot's coefficient	0.75
NFs outside SRV	Compressibility, psi^{-1}	7.5×10^{-6}
	Young's Modulus, psi	1.5×10^{6}
	Poisson's ratio	0.26
	Biot's coefficient	0.75
Matrix	Compressibility, psi^{-1}	5.0×10^{-6}
	Young's Modulus, psi	2.0×10^{6}
	Poisson's ratio	0.26
	Biot's coefficient	0.7

Table 4—Properties of the pseudocomponents of a typical volatile oil in the Eagle Ford Shale

Pseudo-components	Composition	Pc, MPa	Tc, K	Acentric factor	Molar Weight, g/mol
CO_2	0.012	7.376	304.20	0.2250	44.01
N_2	0.002	3.394	126.20	0.0400	28.01
CH_4	0.115	4.600	190.60	0.0080	16.04
C2-5	0.264	3.698	274.74	0.1723	52.02
C6-C10	0.381	2.541	438.68	0.2839	103.01
C11+	0.226	1.778	740.29	0.6716	267.15

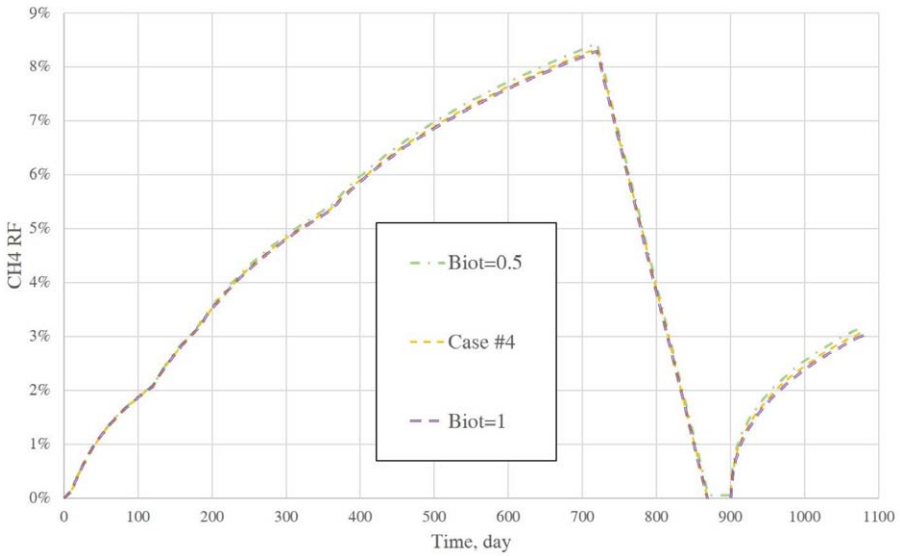

Figure 13—Comparison of the RF of CH_4 component with different Biot's coefficient in fractures

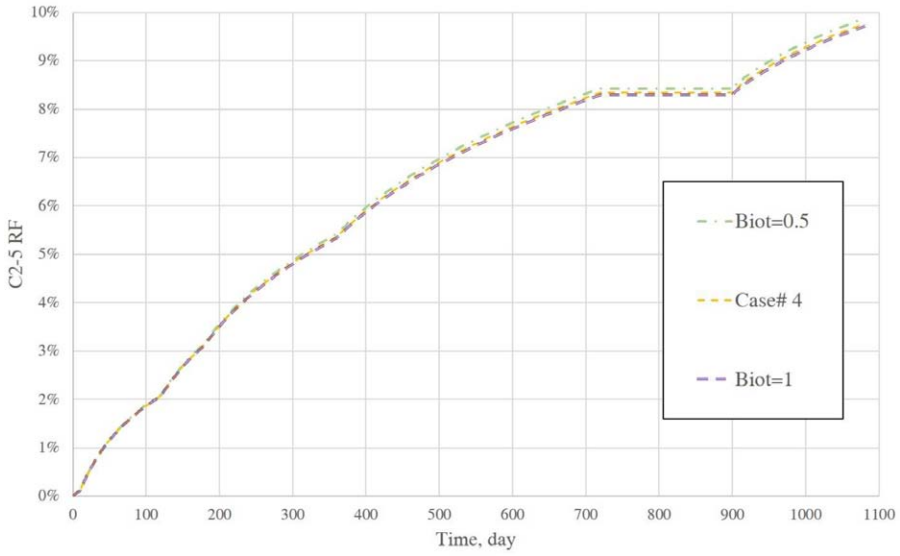

Figure 14—Comparison of the RF of C2-5 component with different Biot's coefficient in fractures

In Case# 9, 10 and 11, different values of Biot's coefficient (α=0.1, 0.4, 1) were specified for the matrix. As shown in Figure 15 and Figure 16, a higher Biot's coefficient would lead to a higher recovery factor for both CH_4 and C2-5 component which is the opposite with the cases in the fracture media. This was because the effect of permeability reduction due to increased effective stress was compensated by a better reduction

of pore volume, i.e. enhanced rock compaction drive. For the gas injection stage, since the injection rate was set as constant, its effect was minimal. However, since less gas was produced in the primary depletion with decreasing Biot's coefficient of the matrix, the RF of CH_4 might become negative as the injected gas volume was slightly higher than the produced volume

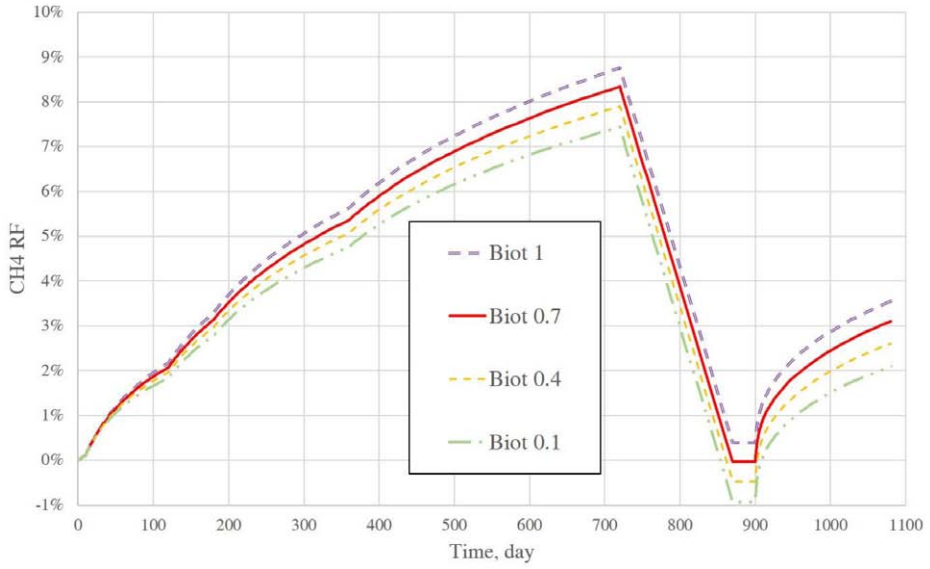

Figure 15—Comparison of the RF of CH_4 component with different Biot's coefficient in the matrix

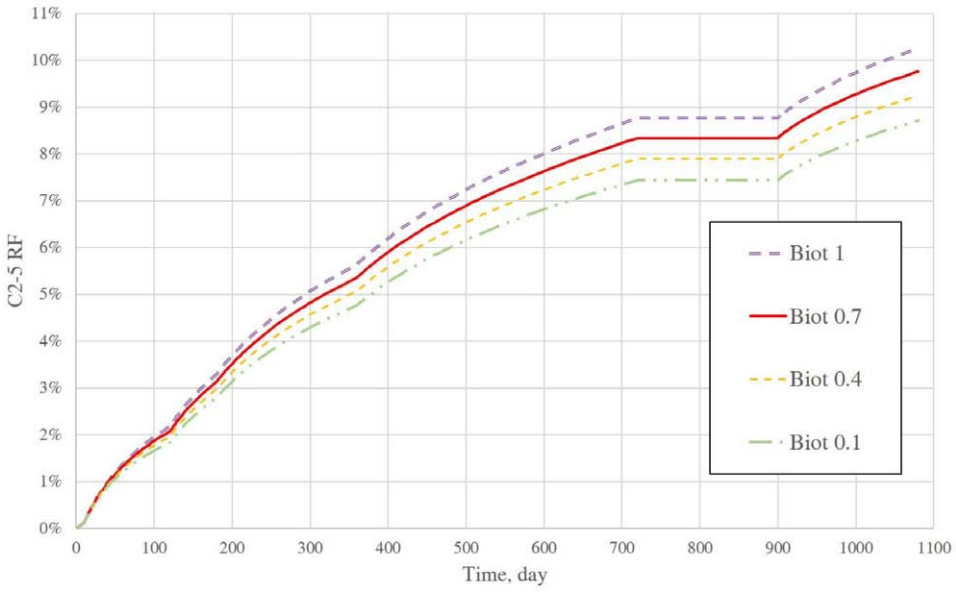

Figure 16—Comparison of the RF of C2-5 component with different Biot's coefficient in the matrix

We have so far discussed the effect of coupling geomechanics and nanopore confinement effect in the depletion and the first cycle of gas huff-n-puff. Below, several representative cases were extended to 3600 days with an additional seven huff-n-puff cycles to study their long-term impacts.

Case# 12 had the same input as Case #2 but extended cycles. Case #13 was the same as Case #12 except the gas injection stage was replaced by well shut-in. Case #12 and #13 both accounted for geomechanics but not nanopore confinement or molecular diffusion. The RF of CH_4 and CO_2 were not shown because they were the components of the injected gas. As shown in Figure 17, each phase had a very similar recovery factor for the primary depletion, this is because the matrix in the reservoir was still above the bubble point.

For the cyclic gas injection case, the RF factor was higher than the primary depletion for every component except CH_4 and CO_2. For the first cycle, each component had a similar RF. In the 2nd-6th cycle, the heavier the component, the higher the RF. After 6 cycles, there was a crossover point around the 3080th day, where the heavier component started to have a lower RF than the lighter component. Finally, the recovery factor of lighter components was higher than the heavier component. One possible reason behind this counterintuitive phenomenon might be that the injected dry gas would first enter the matrix near the fracture network and the equilibrium vapor phase would become richer with intermediate components (C2-5 and C6-10), but it would be further pushed away from the hydraulic fracture. However, when production resumed, due to the existence of critical gas saturation in the matrix, this vapor phase enriched with the intermediate would find it difficult to re-enter the fracture network. The mixing process is like a vaporizing gas drive but with a different flow direction. In a vaporizing gas drive, the injected gas will push the enriched vapor phase towards a producer, but gas injected during huff-n-puff will push the enriched vapor phase away from the hydraulic fracture which acts like a de facto well in this case. The crossover point happened after the reservoir pressure fell below the bubble point pressure, which has been shifted from its original value due to the changed composition. The liberated gas would then overcome this critical gas saturation and pushed that intermediate component towards the hydraulic fracture and finally the light component recovery factor would surpass the heavier component due to the higher gas mobility compared to that of the oil phase rich with C11+.

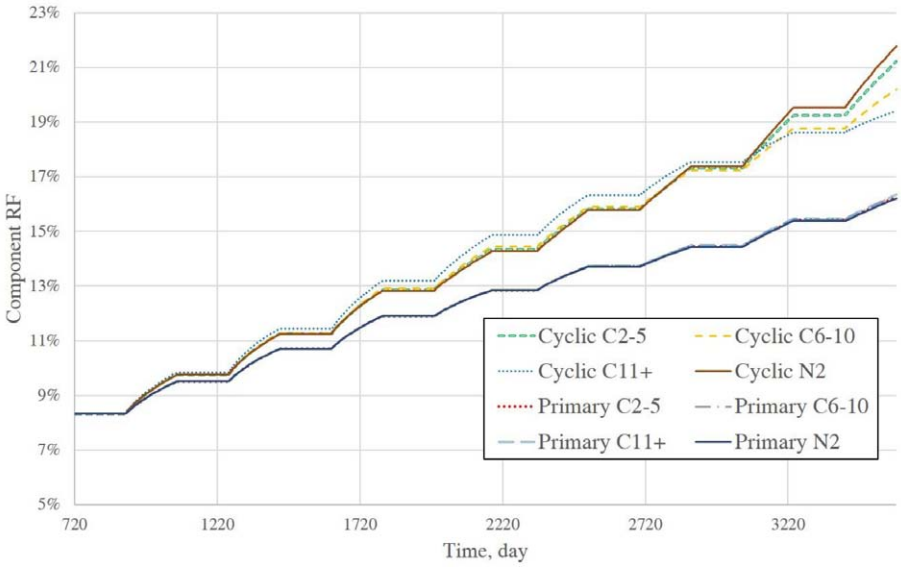

Figure 17—Comparison of the RF between primary production and cyclic gas injection after 10 years

Such a phenomenon is controlled mainly by the critical gas saturation of the matrix. This phenomenon is also partially because of the upstream weighting scheme, where the fracture relative permeability will control the gas injection process and the matrix relative permeability will control the production process. And often the critical gas saturation in fracture was specified as a small value making such phenomenon more significant. In Case #14, by lowering the critical gas saturation from 0.127 to 0.05 in the matrix, the crossover point would appear early around 2360th day which was 720 days ahead of Case #12 as shown in Figure 18.

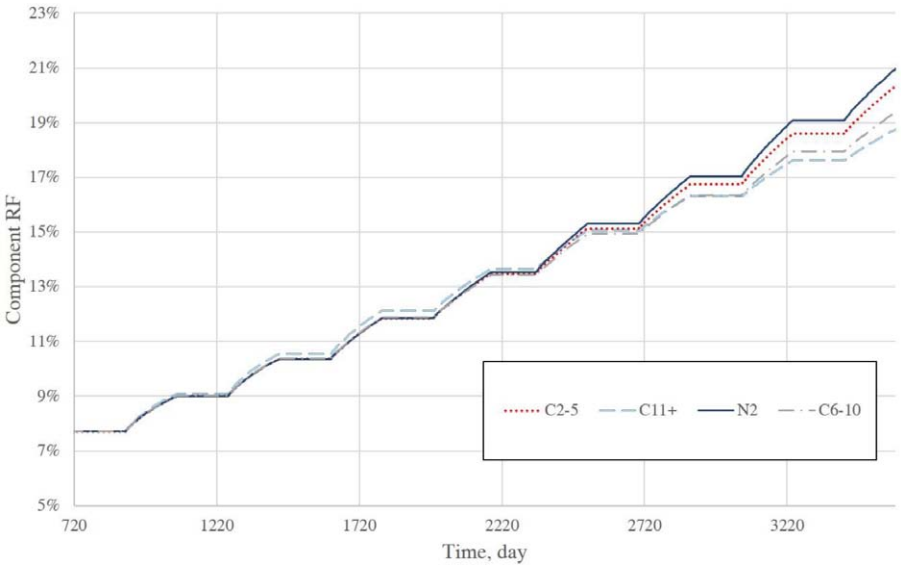

Figure 18—RF of cyclic gas injection with a reduced critical gas saturation in the matrix after 10 years

Case #15 considered coupled nanopore confinement and geomechanics while Case #12 only accounted for the geomechanics. As shown in Figure 19, considering the nanopore confinement effect will slightly delay the crossover point to the 3120th day. However, before the crossover point and starting the 2700th day, the RF difference between Case #12 and Case #15 becomes non-negligible especially for N_2, the nanopore confinement will lower the RF of a lighter component, and slightly increase the RF of a heavier component. This is mainly because the nanopore confinement effect will alter the phase molar composition, i.e. making the trapped gas phase even richer with light and intermediate components and the mobile oil phase leaner with them as mentioned in an earlier study by Wang et al. (2016). More light and intermediate components would be trapped in the matrix's gas phase, which would hence lower its component RF before the crossover point.

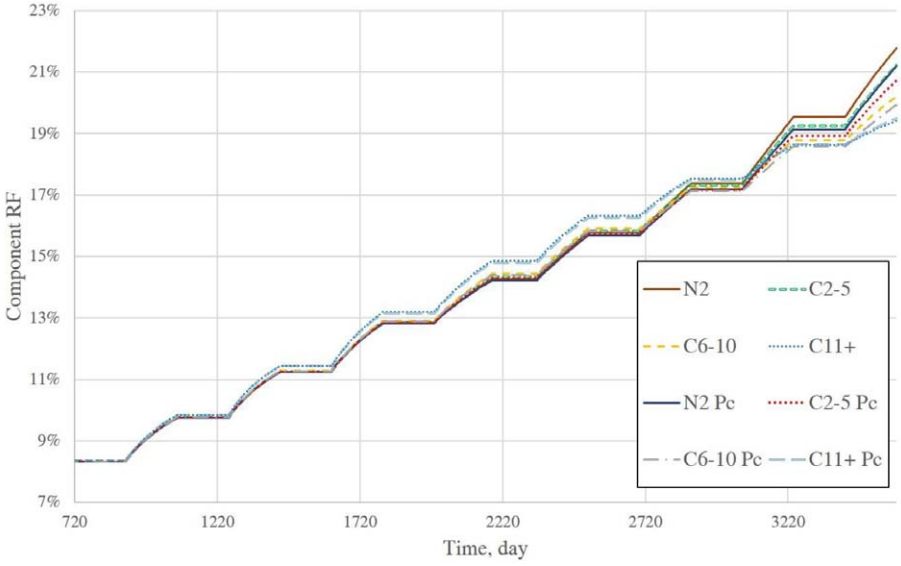

Figure 19—RF of cyclic gas injection with nanopore confinement after 10 years

Conclusions

This study presents a 3D multiphase multicomponent simulator which is a practical tool for accurately modeling primary depletion as well as gas injection IOR/EOR processes in fractured unconventional oil reservoirs. The simulator was first validated against a commercial compositional simulator (CMG-GEM). Then it was applied to study the coupled nanopore confinement and geomechanics effects for the primary depletion and the preceding gas injection in a well located in the black-oil region in the Eagle Ford Shale.

If the reservoir pressure is much higher than the bubble point pressure, the nanopore confinement effect will have a very limited impact on the recovery factor for both the depletion and the first few cycles of gas huff-n-puff.

Geomechanics is a very important factor in production. For the fracture network, a higher Biot's coefficient in the fracture would lead to a larger effective stress change, causing a larger reduction of fracture permeability hence a lower recovery. However, in the matrix, a higher Biot's coefficient would favor the recovery as the enhanced rock compaction drive would offset permeability reduction.

Gas huff-n-puff would improve the component recovery factor compared with primary depletion. A heavier component would first have a higher RF than a lighter component at the first few cycles of huff-n-puff, but its RF would be gradually outpaced by a lighter component after a crossover point. This crossover point is controlled by the critical gas saturation in the matrix.

Lastly, considering the nanopore confinement effects in huff-n-puff would slightly reduce the RF of light components but increase the RF of heavy components before reaching the crossover point. A heavier component's RF will still be surpassed by that of a lighter component, but this crossover point will be delayed due to the nanopore confinement effects.

Acknowledgements

The authors would like to thank Energi Simulation and Research Institute of Petroleum Exploration and Development (RIPED) for providing the financial support to this study. Also, we would like to thank Computer Modelling Group (CMG) for the software which is used in the validation study.

References

Alharthy, N.S., Teklu, T.W.W., Nguyen, T.N., Kazemi, H. and Graves, R.M., 2016. Nanopore Compositional Modeling in Unconventional Shale Reservoirs. *SPE Reservoir Evaluation & Engineering*, **19**(03), pp.415–428.

Chaudhary, A.S., Ehlig-Economides, C.A. and Wattenbarger, R.A., 2011, January. Shale oil production performance from a stimulated reservoir volume. *In SPE Annual Technical Conference and Exhibition*. Society of Petroleum Engineers.

Chen, C., Balhoff, M.T. and Mohanty, K.K., 2014. Effect of Reservoir Heterogeneity on Primary Recovery and CO2 Huff 'n' Puff Recovery in Shale-Oil Reservoirs. *SPE Reservoir Evaluation & Engineering*, **17**(03), pp.404–413.

Cheng, Y., 2012. Impacts of the number of perforation clusters and cluster spacing on production performance of horizontal shale-gas wells. *SPE Reservoir Evaluation & Engineering*, **15**(01), pp.31–40.

Cho, Y., Ozkan, E. and Apaydin, O.G., 2013. Pressure-dependent natural-fracture permeability in shale and its effect on shale-gas well production. *SPE Reservoir Evaluation & Engineering*, **16**(02), pp.216–228.

CMG, 2016. *GEM User's Guide. Computer Modeling Group*.

Danesh, A., 1998. *PVT and phase behaviour of petroleum reservoir fluids* (Vol. **47**). Elsevier.

EIA, 2018. *Annual Energy Outlook* 2018.

Firincioglu, T., Ozkan, E. and Ozgen, C., 2012, January. Thermodynamics of multiphase flow in unconventional liquids-rich reservoirs. In *SPE Annual Technical Conference and Exhibition*. Society of Petroleum Engineers.

Gamadi, T., Elldakli, F. and Sheng, J.J., 2014, August. Compositional simulation evaluation of EOR potential in shale oil reservoirs by cyclic natural gas injection. *In Unconventional Resources Technology Conference*, Denver, Colorado, 25-27 August 2014 (pp. 1625–1639).

Gong, X., Tian, Y., McVay, D.A., Ayers, W.B. and Lee, J., 2013, November. Assessment of Eagle Ford Shale Oil and Gas Resources. *In SPE Unconventional Resources Conference Canada*. Society of Petroleum Engineers.

Guo, X., Wu, K. and Killough, J., 2018. Investigation of Production-Induced Stress Changes for Infill-Well Stimulation in Eagle Ford Shale. *SPE Journal*.

Hawthorne, S.B., Gorecki, C.D., Sorensen, J.A., Steadman, E.N., Harju, J.A. and Melzer, S., 2013, November. Hydrocarbon mobilization mechanisms from upper, middle, and lower Bakken reservoir rocks exposed to CO. *In SPE Unconventional Resources Conference Canada*. Society of Petroleum Engineers.

Hoffman, B.T., Sonnenberg, S., Kazemi, H. and Cui, Q., 2014, August. The Benefits of Reinjecting Instead of Flaring Produced Gas in Unconventional Oil Reservoirs. *In Unconventional Resources Technology Conference*.

Hoffman, B.T. and Evans, J.G., 2016, May. Improved oil recovery IOR pilot projects in the Bakken formation. In *SPE Low Perm Symposium*. Society of Petroleum Engineers.

Katz, D.L., Monroe, R.R. and Trainer, R.P., 1943. Surface tension of crude oils containing dissolved gases. *Petroleum Technology*, **6**(05), pp.1–10.

Kurtoglu, B., Sorensen, J.A., Braunberger, J., Smith, S. and Kazemi, H., 2013, August. Geologic characterization of a Bakken reservoir for potential CO2 EOR. *In Unconventional Resources Technology Conference* (pp. 1834–1844).

McKee, C.R., Bumb, A.C. and Koenig, R.A., 1988. Stress-dependent permeability and porosity of coal and other geologic formations. *SPE formation evaluation*, **3**(01), pp.81–91.

Mokhtari, M., Honarpour, M.M., Tutuncu, A.N. and Boitnott, G.N., 2014, October. Acoustical and Geomechanical Characterization of Eagle Ford Shale-Anisotropy, Heterogeneity and Measurement Scale. *In SPE Annual Technical Conference and Exhibition*. Society of Petroleum Engineers.

Nelson, P.H., 2009. Pore-throat sizes in sandstones, tight sandstones, and shales. *AAPG bulletin*, **93**(3), pp.329–340.

Parsa, E., Yin, X. and Ozkan, E., 2015, September. Direct observation of the impact of nanopore confinement on petroleum gas condensation. In *SPE Annual Technical Conference and Exhibition*. Society of Petroleum Engineers.

Peng, X., Zeng, F., Du, Z. and Yang, H., 2017. Experimental study on pressure control strategies for improving waterflooding potentials in a heavy oil-methane system. *Journal of Petroleum Science and Engineering*, **149**, pp.126–137.

Phi, T. and Schechter, D., 2017, February. CO 2 EOR Simulation in Unconventional Liquid Reservoirs: An Eagle Ford Case Study. In *SPE Unconventional Resources Conference*. Society of Petroleum Engineers.

Pruess, K., 1991. *TOUGH2-A general-purpose numerical simulator for multiphase fluid and heat flow*.

Qiao, C., 2015. *General Purpose Compositional Simulation for Multiphase Reactive Flow with a Fast Linear Solver*.

Sanchez-Rivera, D., Mohanty, K. and Balhoff, M., 2015. Reservoir simulation and optimization of Huff-and-Puff operations in the Bakken Shale. *Fuel*, **147**, pp.82–94.

Shapiro, A.A. and Stenby, E.H., 2001. Thermodynamics of the multicomponent vapor–liquid equilibrium under capillary pressure difference. *Fluid Phase Equilibria*, **178**(1-2), pp.17–32.

Sheng, J.J. and Chen, K., 2014. Evaluation of the EOR potential of gas and water injection in shale oil reservoirs. *Journal of Unconventional Oil and Gas Resources*, **5**, pp.1–9.

Sheng, J.J., 2015. Enhanced oil recovery in shale reservoirs by gas injection. *Journal of Natural Gas Science and Engineering*, **22**, pp.252–259.

Teklu, T.W., Alharthy, N., Kazemi, H., Yin, X., Graves, R.M. and AlSumaiti, A.M., 2014. Phase behavior and minimum miscibility pressure in nanopores. *SPE Reservoir Evaluation & Engineering*, **17**(03), pp.396–403.

Tian, Y., 2014, October. Experimental study on stress sensitivity of naturally fractured reservoirs. In *SPE Annual Technical Conference and Exhibition*. Society of Petroleum Engineers.

Tian, Y., Yu, X., Li, J., Neeves, K.B., Yin, X. and Wu, Y.S., 2019. Scaling law for slip flow of gases in nanoporous media from nanofluidics, rocks, and pore-scale simulations. *Fuel*, **236**, pp.1065–1077.

Uzun, I., Eker, E., Kazemi, H. and Stoltz, R.P., 2018, April. An Efficient Compositional Model for Unconventional Reservoirs: Eagle Ford Formation Case Study. *In SPE Western Regional Meeting*. Society of Petroleum Engineers.

Wan, T., Sheng, J., Soliman, M.Y. and Zhang, Y., 2016. Effect of fracture characteristics on behavior of fractured shale-oil reservoirs by cyclic gas injection. *SPE Reservoir Evaluation & Engineering*, **19**(02), pp.350–355.

Wang, J.S.Y. and Narasimhan, T.N., 1985. Hydrologic mechanisms governing fluid flow in a partially saturated, fractured, porous medium. *Water Resources Research*, **21**(12), pp.1861–1874.

Wang, L., Parsa, E., Gao, Y., Ok, J.T., Neeves, K., Yin, X. and Ozkan, E., 2014, April. Experimental study and modeling of the effect of nanoconfinement on hydrocarbon phase behavior in unconventional reservoirs. *In SPE Western North American and Rocky Mountain Joint Meeting*. Society of Petroleum Engineers.

Wang, L., Yin, X., Neeves, K.B. and Ozkan, E., 2016. Effect of pore-size distribution on phase transition of hydrocarbon mixtures in nanoporous media. *SPE Journal*, **21**(06), pp.1–981.

Wang, L., Tian, Y., Yu, X., Wang, C., Yao, B., Wang, S., Winterfeld, P.H., Wang, X., Yang, Z., Wang, Y. and Cui, J., 2017. Advances in improved/enhanced oil recovery technologies for tight and shale reservoirs. *Fuel*, **210**, pp.425–445.

Weinaug, C.F. and Katz, D.L., 1943. Surface tensions of methane-propane mixtures. *Industrial & Engineering Chemistry*, **35**(2), pp.239–246.

Whitson, C.H. and Michelsen, M.L., 1989. The negative flash. *Fluid Phase Equilibria*, **53**, pp.51–71.

Winterfeld, P.H. and Wu, Y.S., 2016. Simulation of Coupled Thermal/Hydrological/Mechanical Phenomena in Porous Media. *SPE Journal*, **21**(03), pp.1–041.

Winterfeld, P.H. and Wu, Y.S., 2018. *Quantitative Characterization of Impacts of Coupled Geomechanics and Flow on Safe and Permanent Geological Storage of CO2 in Fractured Aquifers: Final Report (No. DE-FE0023305)*. Colorado School of Mines, Golden, CO (United States).

Wu, Y.S. and Pruess, K., 1988. A Multiple-Porosity Method for Simulation of Naturally Fractured Petroleum Reservoirs. *SPE Reservoir Engineering*, **3**(01), pp.327–336.

Wu, Y.S., 2015. *Multiphase fluid flow in porous and fractured reservoirs*. Gulf Professional Publishing.

Xiong, Y., 2015. *Development of a compositional model fully coupled with geomechanics and its application to tight oil reservoir simulation*.

Yu, W., Lashgari, H.R., Wu, K. and Sepehrnoori, K., 2015. CO2 injection for enhanced oil recovery in Bakken tight oil reservoirs. *Fuel*, **159**, pp.354–363.

Yu, W., Zhang, Y., Varavei, A., Sepehrnoori, K., Zhang, T., Wu, K. and Miao, J., 2018, April. Compositional Simulation of CO2 Huff-n-Puff in Eagle Ford Tight Oil Reservoirs with CO2 Molecular Diffusion, Nanopore Confinement and Complex Natural Fractures. In *SPE Improved Oil Recovery Conference*. Society of Petroleum Engineers.

Zoback, M.D., 2010. *Reservoir Geomechanics*. Cambridge University Press.